

Nonlinear harmonic generation and devices in doubly resonant Kerr cavities

Hila Hashemi,¹ Alejandro W. Rodriguez,² J. D. Joannopoulos,² Marin Soljačić,² and Steven G. Johnson¹

¹*Department of Mathematics, Massachusetts Institute of Technology, Cambridge, Massachusetts 02139, USA*

²*Department of Physics, Massachusetts Institute of Technology, Cambridge, Massachusetts 02139, USA*

(Received 3 August 2008; revised manuscript received 27 October 2008; published 13 January 2009)

We describe a theoretical analysis of the nonlinear dynamics of third-harmonic generation ($\omega \rightarrow 3\omega$) via Kerr ($\chi^{(3)}$) nonlinearities in a resonant cavity with resonances at both ω and 3ω . Such a doubly resonant cavity greatly reduces the required power for efficient harmonic generation, by a factor of $\sim V/Q^2$, where V is the modal volume and Q is the lifetime, and can even exhibit 100% harmonic conversion efficiency at a critical input power. However, we show that it also exhibits a rich variety of nonlinear dynamics, such as multistable solutions and long-period limit cycles. We describe how to compensate for self- and cross-phase modulation (which otherwise shifts the cavity frequencies out of resonance), and how to excite the different stable solutions (and especially the high-efficiency solutions) by specially modulated input pulses.

DOI: 10.1103/PhysRevA.79.013812

PACS number(s): 42.65.Ky, 42.60.Da, 42.65.Sf, 42.65.Jx

I. INTRODUCTION

In this paper, we describe how 100% third-harmonic conversion can occur in doubly resonant optical cavities with Kerr nonlinearities, even when dynamical stability and self-phase modulation (which can drive the cavities out of resonance) are included (extending our earlier work [1]), and describe the initial conditions required to excite these efficient solutions. In particular, we show that such doubly-resonant nonlinear optical systems can display a rich variety of dynamical behaviors, including multistability (different steady states excited by varying initial conditions, a richer version of the bistable phenomenon observed in single-mode cavities [2]), gap solitons [3], long-period limit cycles (similar to the “self-pulsing” observed for second-harmonic generation [4,5]), and transitions in the stability and multiplicity of solutions as the parameters are varied. One reason for studying such doubly resonant cavities was the fact that they lower the power requirements for nonlinear devices [1], and in particular for third harmonic conversion, compared to singly resonant cavities or nonresonant structures [6–23]. An appreciation and understanding of these behaviors is important to design efficient harmonic converters (the main focus of this paper), but it also opens the possibility of new types of devices enabled by other aspects of the nonlinear dynamics. For example, strong Kerr nonlinearities are desired in the context of quantum information theory for use in low-loss photon entanglement and other single-photon applications [24–28].

In a Kerr ($\chi^{(3)}$) medium, there is a change in the refractive index proportional to the square of the electric field; for an oscillating field at a frequency ω , this results in a shift in the index at the same frequency [self-phase modulation (SPM)], generation of power at the third-harmonic frequency 3ω , and also other effects when multiple frequencies are present [cross-phase modulation (XPM) and four-wave mixing (FWM)] [29]. When the field is confined in a cavity, restricted to a small modal volume V for a long time given by the quality factor Q (a lifetime in units of the optical period) [30], such nonlinear effects are enhanced by both the increased field strength for the same input power and by the

frequency sensitivity inherent in resonant effects (since the fractional bandwidth is $1/Q$). This enhancement is exploited, for example, in nonlinear harmonic and sum-frequency generation, most commonly for $\chi^{(2)}$ effects where the change in index is proportional to the electric field (which requires a noncentrosymmetric material) [29]. One can further enhance harmonic generation by using a cavity with two resonant modes, one at the source frequency and one at the harmonic frequency [4,31–38]. In this case, one must also take into account a nonlinear down-conversion process that competes with harmonic generation [4,37,38], but it turns out to be theoretically possible to obtain 100% harmonic conversion for either $\chi^{(2)}$ ($\omega \rightarrow 2\omega$) or $\chi^{(3)}$ ($\omega \rightarrow 3\omega$) nonlinearities at a specific “critical” input power P_{crit} (both in a one-dimensional model of propagating waves for $\chi^{(2)}$ nonlinearities [39] and also in a more general coupled-mode model for either $\chi^{(2)}$ or $\chi^{(3)}$ nonlinearities [1]). In particular, we studied the harmonic-generation and down-conversion processes in a broad class of model systems depicted in Fig. 1: a single input channel (e.g., a waveguide) is coupled to a nonlinear cavity with two resonant frequencies, where both reflected and harmonic fields are emitted back into the input channel.

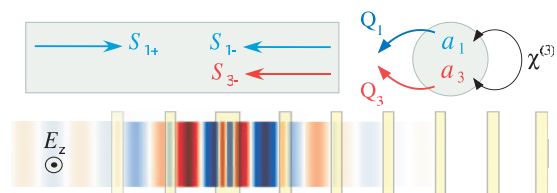


FIG. 1. (Color) Top: Schematic of general scheme for third-harmonic generation and dynamical variables for coupled-mode equations: a single input (output) channel [with incoming (outgoing) field amplitudes s_{\pm}] is coupled to a resonant cavity with two modes at frequencies ω_1 and $3\omega_1$ (and corresponding amplitudes a_1 and a_3). The two resonant modes are nonlinearly coupled by a Kerr ($\chi^{(3)}$) nonlinearity. Bottom: An example realization [1], in one dimension, using a semi-infinite quarter-wave stack of dielectric layers with a doubled-layer defect (resonant cavity) that is coupled to incident plane waves; the electric field of a steady-state $3\omega_1$ solution is shown as blue, white, and red for negative, zero, and positive, respectively.

In this case, we predicted 100% harmonic generation at a critical power P_{crit} proportional to V/Q^3 for $\chi^{(2)}$ and V/Q^2 for $\chi^{(3)}$ [1]. However, we only looked at the steady-state solution of the system and not its dynamics or stability. Moreover, in the $\chi^{(3)}$ case there can also be an SPM and XPM effect that shifts the cavity frequencies out of resonance and spoils the harmonic-generation effect. In this paper, we consider both of these effects, describe how to compensate for SPM and XPM, and demonstrate the different regimes of stability in such $\chi^{(3)}$ doubly resonant systems. We show that the parameters and the initial conditions must be chosen within certain regimes to obtain a stable steady state with high conversion efficiency.

In other regimes, we demonstrate radically different behaviors: not only low-efficiency steady states, but also limit-cycle solutions where the efficiency oscillates slowly with a repetition period of many thousands of optical cycles. With infrared light, these limit cycles form a kind of optical oscillator (clock) with a period in the hundreds of GHz or THz (and possibly lower, depending on the cavity parameters). Previously, limit-cycle (self-pulsing) behaviors have been observed in a number of other nonlinear optical systems, such as doubly resonant $\chi^{(2)}$ cavities coupled by second-harmonic generation [4]; bistable multimode Kerr cavities with time-delayed nonlinearities [40]; nonresonant distributed feedback in Bragg gratings [41]; and a number of nonlinear lasing devices [42]. However, the system considered in this work seems unusually simple, especially among $\chi^{(3)}$ systems, in that it only requires two modes and an instantaneous Kerr nonlinearity, with a constant-frequency input source, to attain self-pulsing, and partly as a consequence of this simplicity the precise self-pulsing solution is quite insensitive to the initial conditions. In other nonlinear optical systems where self-pulsing was observed, other authors have also observed chaotic solutions in certain regimes. Here, we did not observe chaos for any of the parameter regimes considered, where the input was a constant-frequency source, but it is possible that chaotic solutions may be excited by an appropriate pulsed input as in the $\chi^{(2)}$ case [4,5].

Another interesting phenomenon that can occur in nonlinear systems is multistability, where there are multiple possible steady-state solutions that one can switch among by varying the initial conditions. In Kerr ($\chi^{(3)}$) media, an important example of this phenomenon is bistable transmission through nonlinear cavities: for transmission through a single-mode cavity, output can switch discontinuously between a high-transmission and a low-transmission state in a hysteresis effect that results from SPM [2]. For example, if one turns on the power gradually from zero the system stays in the low-transmission state, but if the power is increased further and then decreased to the original level, the system can be switched to the high-transmission state. This effect, which has been observed experimentally [43], can be used for all-optical logic, switching, rectification, and many other functions [2]. In a cavity with multiple closely spaced resonances, where the nonlinearity is strong enough to shift one cavity mode's frequency to another's, the same SPM phenomenon can lead to more than two stable solutions [44]. Here, we demonstrate a much richer variety of multistable phenomena in the doubly resonant case for widely separated

cavity frequencies coupled by harmonic generation in addition to SPM—not only can there be more than two stable states, but the transitions between them can exhibit complicated oscillatory behaviors as the initial conditions are varied, and there are also Hopf bifurcations into self-pulsing solutions.

The remaining part of the paper is structured as follows. In Sec. II, we review the theoretical description of harmonic generation in a doubly resonant cavity coupled to input and output waveguides, based on temporal coupled-mode theory, and demonstrate the possibility of 100% harmonic conversion. We also discuss how to compensate for frequency shifting due to SPM and XPM by preshifting the cavity frequencies. In Sec. III, we analyze the stability of this 100%-efficiency solution, and demonstrate the different regimes of stable operation that are achieved in practice starting from that theoretical initial condition. We also present bifurcation diagrams that show how the stable and unstable solutions evolve as the parameters vary. Finally, in Sec. IV, we consider how to excite these high-efficiency solutions in practice, by examining the effect of varying initial conditions and uncertainties in the cavity parameters. In particular, we demonstrate the multistable phenomena exhibited as the initial conditions are varied. We close with some concluding remarks, discussing the many potential directions for future work that are revealed by the phenomena described here.

II. 100% HARMONIC CONVERSION IN DOUBLY RESONANT CAVITIES

In this section, we describe the basic theory of frequency conversion in doubly resonant cavities with $\chi^{(3)}$ nonlinearities, including the undesirable self- and cross-phase modulation effects, and explain the existence of a solution with 100% harmonic conversion (without considering stability). Consider a waveguide coupled to a doubly resonant cavity with two resonant frequencies $\omega_1^{\text{cav}} = \omega_1$ and $\omega_3^{\text{cav}} = \omega_3 = 3\omega_1$ (below, we will shift ω_k^{cav} to differ slightly from ω_k), and corresponding lifetimes τ_1 and τ_3 describing their radiation rates into the waveguide (or quality factors $Q_k = \omega_k \tau_k / 2$). In addition, these modes are coupled to one another via the Kerr nonlinearity. Because all of these couplings are weak, any such system (regardless of the specific geometry), can be accurately described by temporal coupled-mode theory, in which the system is modeled as a set of coupled ordinary differential equations representing the amplitudes of the different modes, with coupling constants and frequencies determined by the specific geometry [1,45]. In particular, the coupled-mode equations for this particular class of geometries were derived in Ref. [1] along with explicit equations for the coupling coefficients in a particular geometry. The degrees of freedom are the field amplitude a_k of the k th cavity mode (normalized so that $|a_k|^2$ is the corresponding energy) and the field amplitude $s_{k\pm}$ of the incoming (+) and outgoing (−) waveguide modes at ω_k (normalized so that $|s_{k\pm}|^2$ is the corresponding power), as depicted schematically in Fig. 1. These field amplitudes are coupled by the following equations (assuming that there is only input at ω_1 , i.e., $s_{3+} = 0$):

$$\dot{a}_1 = \left[i\omega_1^{\text{cav}}(1 - \alpha_{11}|a_1|^2 - \alpha_{13}|a_3|^2) - \frac{1}{\tau_1} \right] a_1 - i\omega_1\beta_1(a_1^*)^2 a_3 + \sqrt{\frac{2}{\tau_{s,1}}} s_{1+}, \quad (1)$$

$$\dot{a}_3 = \left[i\omega_3^{\text{cav}}(1 - \alpha_{31}|a_1|^2 - \alpha_{33}|a_3|^2) - \frac{1}{\tau_3} \right] a_3 - i\omega_3\beta_3 a_1^3. \quad (2)$$

As explained in Ref. [1], the α and β coefficients are geometry and material-dependent constants that express the strength of various nonlinear effects for the given modes. The α_{ij} terms describe self- and cross-phase modulation effects: they clearly give rise to effective frequency shifts in the two modes. The β_i term characterize the energy transfer between the modes: the β_3 term describes frequency up-conversion and the β_1 term describes down-conversion. As shown in Ref. [1], they are related to one another via conservation of energy $\omega_1\beta_1 = \omega_3\beta_3^*$, and all of the nonlinear coefficients scale inversely with the modal volume V .

There are three different α_{ij} parameters (two SPM coefficients α_{11} and α_{33} and one XPM coefficient $\alpha_{13} = \alpha_{31}$). All three values are different, in general, but are determined by similar integrals of the field patterns, produce similar frequency-shifting phenomena, and all scale as $1/V$. Therefore, in order to limit the parameter space analyzed in this paper, we consider the simplified case where all three frequency-shifting terms have the same strength $\alpha_{ij} = \alpha$.

One can also include various losses, e.g., linear losses correspond to a complex ω_1 and/or ω_3 , and nonlinear two-photon absorption corresponds to a complex α . As discussed in the concluding remarks, however, we have found that such considerations do not qualitatively change the results (only reducing the efficiency somewhat, as long as the losses are not too big compared to the radiative lifetimes τ), and so in this manuscript we restrict ourselves to the idealized lossless case.

Figure 2 shows the steady-state conversion efficiency ($|s_{3-}|^2/|s_{1+}|^2$) versus input power of light that is incident on the cavity at ω_1^{cav} , for the same parameter regime in Ref. [1] (i.e., assuming negligible self- and cross-phase modulation so that $\alpha=0$), and not considering the stability of the steady state. As shown by the solid red curve, as one increases the input power $|s_{1+}|^2$, the efficiency increases, peaking at 100% conversion for a critical $P_{\text{crit}} = |s_{1+}^{\text{crit}}|^2$, where

$$|s_{1+}^{\text{crit}}|^2 = \left(\frac{4}{|\omega_1\beta_1|^2 \tau_3^3} \right)^{1/4}. \quad (3)$$

The efficiency decreases if the power is either too low (in the linear regime) or too high (dominated by down-conversion). The critical input power $|s_{1+}^{\text{crit}}|^2$ scales as V/Q^2 , so one can in principle obtain very low-power efficient harmonic conversion by increasing Q and/or decreasing V [1]. Including absorption or other losses decreases the peak efficiency, but does not otherwise qualitatively change this solution [1].

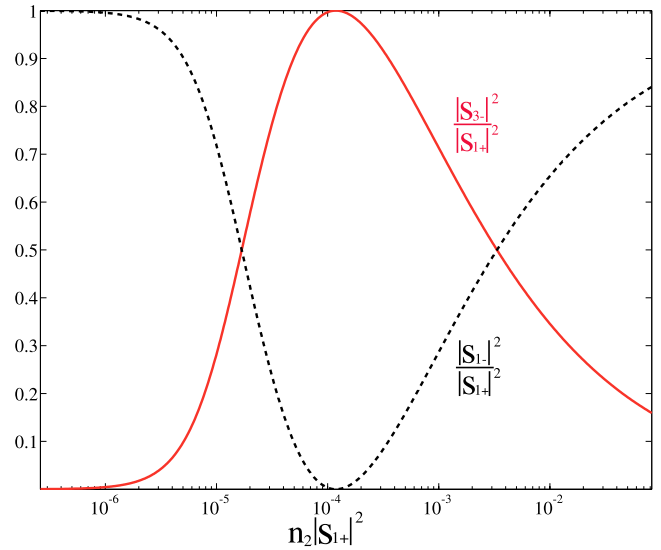


FIG. 2. (Color online) Steady-state efficiency of third-harmonic generation (solid red line) from Ref. [1], for $\alpha=0$ (no self-phase modulation), as a function of input power $|s_{1+}|^2$ scaled by the Kerr coefficient $n_2 = 3\chi^{(3)}/4c\epsilon$. The reflected power at the incident frequency ω_1 is shown as a dashed black line. There is a critical power where the efficiency of harmonic generation is 100. The parameters used in this plot are $Q_1=1000$, $Q_3=3000$, $\beta_1 = (4.55985 - 0.7244i) \times 10^{-5}$ in dimensionless units of $\chi^{(3)}/V\epsilon$.

There are two effects that we did not previously analyze in detail, however, which can degrade this promising solution: nonlinear frequency shifts and instability. Here, we first consider frequency shifts, which arise whenever $\alpha \neq 0$, and consider stability in the next section. The problem with the α terms is that efficient harmonic conversion depends on the cavities being tuned to harmonic frequencies $\omega_3 = 3\omega_1$; a nonlinear shift in the cavity frequencies due to self- and cross-phase modulation will spoil this resonance. In principle, there is a straightforward solution to this problem, as depicted in Fig. 3. Originally (for $\alpha=0$), the cavity was designed to have the frequency ω_1 in the linear regime, but with $\alpha \neq 0$ the effective cavity frequency ω_1^{NL} (including self- and cross-phase modulation terms) is shifted away from the design frequency as shown by the blue line. Instead, we can simply design the linear cavity to have a frequency ω_1^{cav} slightly different from the operating frequency ω_1 , so that self- and cross-phase modulation shifts ω_1^{NL} exactly to ω_1 at the critical input power, as depicted by the green line in Fig. 3. Exactly the same strategy is used for ω_3^{NL} , by preshifting ω_3^{cav} .

More precisely, to compute the required amount of preshifting, we examine the coupled-mode equations (1) and (2). First, we solve P_{crit} assuming $\alpha=0$, as in Ref. [1], and obtain the corresponding critical cavity fields a_k^{crit} .

$$|a_1^{\text{crit}}|^2 = \left(\frac{1}{\omega_1^2 |\beta_1|^2 \tau_3 \tau_{1,s}} \right)^{1/2}, \quad (4)$$

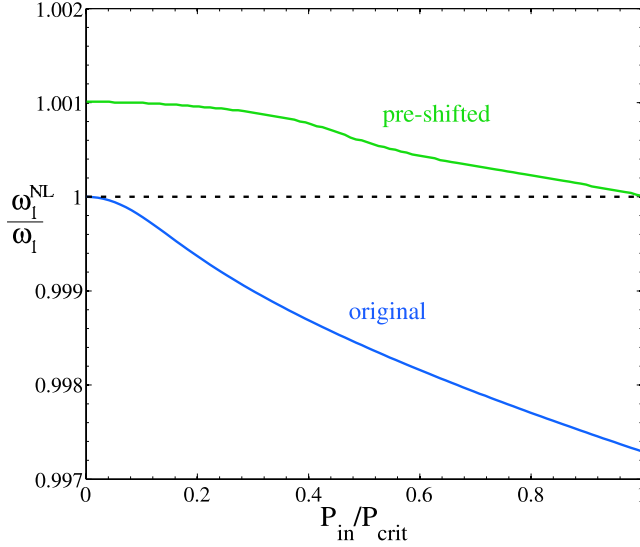


FIG. 3. (Color online) Shift in the resonant frequency ω_1^{NL} as a function of input power, due to self- and cross-phase modulation. (There is an identical shift in ω_3^{NL} .) If the cavity is designed so that the linear ($P_{\text{in}} \rightarrow 0$) frequencies are harmonics, the nonlinearity pushes the system out of resonance (lower blue line) as the power increases to the critical power for 100% efficiency. This is corrected by preshifting the cavity frequencies (upper green line) so that the nonlinear frequency shift pushes the modes into resonance at P_{crit} .

$$|a_3^{\text{crit}}|^2 = \left(\frac{\omega_3 \beta_3 \tau_3}{(\omega_1 \beta_1 \tau_{1,s})^3} \right)^{1/2}. \quad (5)$$

Then, we substitute these critical fields into the coupled-mode equations for $\alpha \neq 0$, and solve for the new cavity frequencies ω_k^{cav} so as to cancel the α terms and make the a_k^{crit} solutions still valid. This yields the following transformation of the cavity frequencies:

$$\omega_1^{\text{cav}} = \frac{\omega_1}{1 - \alpha_{11}|a_1^{\text{crit}}|^2 - \alpha_{13}|a_3^{\text{crit}}|^2}, \quad (6)$$

$$\omega_3^{\text{cav}} = \frac{\omega_3}{1 - \alpha_{13}|a_1^{\text{crit}}|^2 - \alpha_{33}|a_3^{\text{crit}}|^2}. \quad (7)$$

By inspection, when substituted into Eqs. (1) and (2) at the critical power, these yield the same steady-state solution as for $\alpha=0$. (There are two other appearances of ω_1 and ω_3 in the coupled-mode equations, in the β_k terms, but we need not change these frequencies because that is a higher-order effect, and the derivation of the coupled-mode equations considered only first-order terms in $\chi^{(3)}$.)

The nonlinear dynamics turn out to depend only on four dimensionless parameters $\tau_3/\tau_1 = Q_3/3Q_1$, α_{11}/β_1 , α_{33}/β_1 , and $\alpha_{13}/\beta_1 = \alpha_{31}/\beta_1$. The overall scale of Q , α , etcetera, merely determines the absolute scale for the power requirements: it is clear from the equations that multiplying all α and β coefficients by an overall constant K can be compensated by dividing all a and s amplitudes by \sqrt{K} [which happens automatically for s at the critical power by Eq. (3)]; the case of scaling $\tau_{1,3}$ by an overall constant is more subtle and is considered below. As mentioned above, for simplicity we

take $\alpha_{11} = \alpha_{33} = \alpha_{13} = \alpha_{31} = \alpha$. Therefore, in the subsequent sections we will analyze the asymptotic efficiency as a function of τ_3/τ_1 and α/β_1 .

So far, we have found a steady-state solution to the coupled-mode equations, including self- and cross-phase modulation, that achieves 100% third-harmonic conversion. In the following sections, we consider under what conditions this solution is stable, what other stable solutions exist, and for what initial conditions the high-efficiency solution is excited.

To understand the dynamics and stability of the nonlinear coupled-mode equations, we apply the standard technique of identifying fixed points of the equations and analyzing the stability of the linearized equations around each fixed point [46]. By a ‘‘fixed point,’’ we mean a steady-state solution corresponding to an input frequency ω_1 ($s_{1+} \sim e^{i\omega_1 t}$) and hence $a_1(t) = A_1 e^{i\omega_1 t}$ and $a_3(t) = A_3 e^{i3\omega_1 t}$ for some unknown constants A_1 and A_3 . [An input frequency ω_1 can also generate higher harmonics, such as $9\omega_1$ or $5\omega_1$, but these are negligible: both because they are higher-order effects ($\sim [\chi^{(3)}]^2$, and all such terms were dropped in deriving the coupled-mode equations), and because we assume there is no resonant mode present at those frequencies.] By substituting this steady-state form into Eqs. (1) and (2), one obtains two coupled polynomial equations whose roots are the fixed points. We already know one of the fixed points from the previous section, the 100% efficiency solution, but to fully characterize the system one would like to know all of the fixed points (both stable and unstable). We solved these polynomial equations using MATHEMATICA, which is able to compute all of the roots, but some transformations were required to put the equations into a solvable form, as explained in more detail in the Appendix.

As mentioned above, the dynamics are independent of the overall scale of $\tau_{1,3}$, and depend only on the ratio τ_3/τ_1 . This can be seen from the equations for $A_{1,3}$, in which the $\omega_{1,3}$ oscillation has been removed. In these equations, if we multiply τ_1 and τ_3 by an overall constant factor K , after some algebra it can be shown that the $A_{1,3}$ equations are invariant if we rescale $A_1 \rightarrow A_1/\sqrt{K}$, $A_3 \rightarrow A_3/\sqrt{K}$, rescale time $t \rightarrow Kt$, and rescale the input $s_{1+} \rightarrow s_{1+}/K$ [which happens automatically for the critical power by Eq. (3)]. Note also that the conversion efficiency $|s_{3-}/s_{1+}|^2 = (2/\tau_3)|A_3/s_{1+}|^2$ is also invariant under this rescaling by K . That is, the powers and the time scales of the dynamics change if you change the lifetimes, unsurprisingly, but the steady states, stability, etc. (as investigated in the next section) are unaltered.

III. STABILITY AND DYNAMICS

Given the steady-state solutions (the roots), their stability is determined by linearizing the original equations around these points to a first-order linear equation of the form $dx/dt = Ax$; a stable solution is one for which the eigenvalues of A have negative real parts (leading to solutions that decay exponentially towards the fixed point) [46]. The results of this fixed-point and stability analysis are shown in Fig. 4 as a ‘‘phase diagram’’ of the system as a function of the relative lifetimes $\tau_3/\tau_1 = 3Q_3/Q_1$ and the relative strength of self-

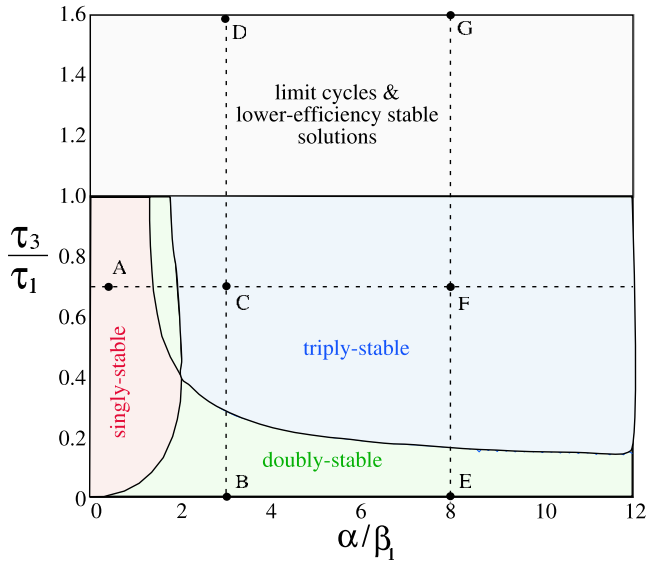


FIG. 4. (Color online) Phase diagram of the nonlinear dynamics of the doubly resonant nonlinear harmonic generation system from Fig. 1 as a function of the relative cavity lifetimes ($\tau_3/\tau_1 = 3Q_3/Q_1$) and the relative strength of SPM and XPM vs harmonic generation (α/β_1) for input power equal to the critical power for 100% efficiency. For $\tau_3 < \tau_1$ there is always one stable 100%-efficiency solution, and for nonzero α the system may have additional stable solutions. For $\tau_3 > \tau_1$ the 100%-efficiency solution becomes unstable, but there are limit cycles and lower-efficiency stable solutions. Various typical points A-G in each region are labeled for reference in the subsequent figures.

phase-modulation vs four-wave mixing α/β_1 . Our original 100%-efficiency solution is always present, but is only stable for $\tau_3 < \tau_1$ and becomes unstable for $\tau_3 > \tau_1$. The transition point, $\tau_3 = \tau_1$, corresponds to equal energy $|a_1|^2 = |a_3|^2$ in the fundamental and harmonic mode at the critical input power. The unstable region corresponds to $|a_3|^2 > |a_1|^2$ (and the down-conversion term is stronger than the up-conversion term)—intuitively, this solution is unstable because, if any perturbation causes the energy in the harmonic mode to decrease, there is not enough pumping from up-conversion to bring it back to the 100%-efficiency solution. Conversely, in the stable $|a_3|^2 < |a_1|^2$ ($\tau_3 < \tau_1$) regime, the higher-energy fundamental mode is being directly pumped by the input and can recover from perturbations. Furthermore, as α/β_1 increases, additional lower-efficiency stable solutions are introduced, resulting in regimes with two (doubly stable) and three (triply stable) stable fixed points. These different regimes are explored in more detail via bifurcation diagrams below, and the excitation of the different stable solutions is considered in the next section.

For $\tau_3 > \tau_1$, the 100%-efficiency solution is unstable, but there are lower-efficiency steady-state solutions and also another interesting phenomenon: limit cycles. A limit cycle is a stable oscillating-efficiency solution, one example of which (corresponding to point D in Fig. 4) is plotted as a function of time in Fig. 5. (In general, the existence of limit cycles is difficult to establish analytically [46], but the phenomenon is clear in the numerical solutions as a periodic oscillation insensitive to the initial conditions). In fact, as we shall see

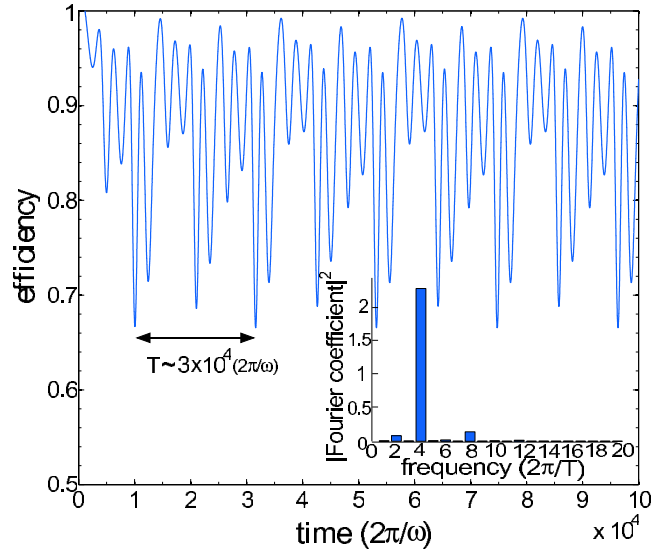


FIG. 5. (Color online) An example of a limit-cycle solution, with a periodically oscillating harmonic-generation efficiency as a function of time, corresponding to point D in Fig. 4. Perturbations in the initial conditions produce only phase shifts in the asymptotic cycle. Here, the limit cycle has a period of around 3×10^4 optical cycles. Inset: Square of Fourier amplitudes (arbitrary units) for each harmonic component of the limit cycle in the Fourier-series expansion of the A_3 .

below, these limit cycles result from a “Hopf bifurcation,” which is a transition from a stable fixed point to an unstable fixed point and a limit cycle [47]. In this example at point D, the efficiency oscillates between roughly 66% and nearly 100%, with a period of several thousand optical cycles. As a consequence of the time scaling described in the last paragraph of the previous section, the period of such limit cycles is proportional to the τ 's. If the frequency ω_1 were $1.55 \mu\text{m}$, for a Q_1 of 500 optical cycles, this limit cycle would have a frequency of around 70 GHz, forming an interesting type of optical “clock” or oscillator. Furthermore, the oscillation is not sinusoidal and contains several higher harmonics as shown in the inset of Fig. 5; the dominant frequency component in this case is the fourth harmonic (~ 280 GHz), but different points in the phase diagram yield limit cycles with different balances of Fourier components.

To better understand the phase diagram of Fig. 4, it is useful to plot the efficiencies of both the stable and unstable solutions as a function of various parameters. Several of these bifurcation diagrams (in which new fixed points typically appear in stable-unstable pairs) are shown in Figs. 6–8. To begin with, Figs. 6 and 7 correspond to lines connecting the labeled points ACF, BCD, and ECG, respectively, in Fig. 4, showing how the stability changes as a function of α/β_1 and τ_3/τ_1 . Figure 6 shows how first one then two new stable fixed points appear as α/β_1 is increased, one approaching zero efficiency and the other closer to 50%. Along with these two stable solutions appear two unstable solutions (dashed lines). (A similar looking plot, albeit inverted, can be found in Ref. [44] for SPM-coupled closely spaced resonances.) In particular, the fact that one of the unstable solutions approaches the 100%-efficiency stable solution causes the latter

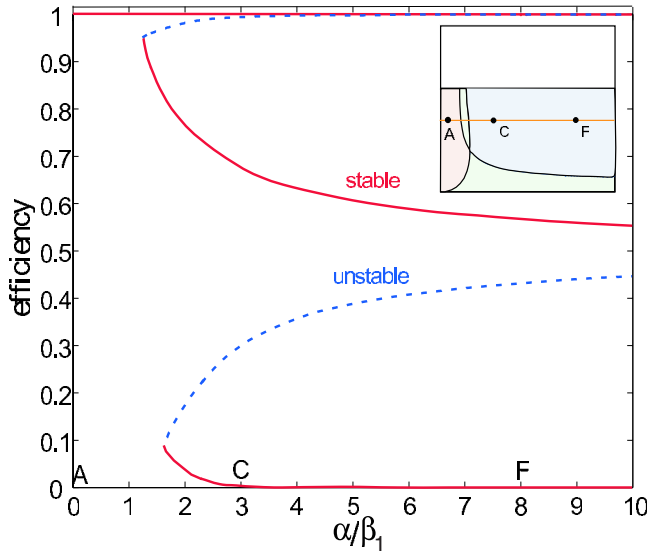


FIG. 6. (Color online) Bifurcation diagram showing the harmonic-generation efficiency of the stable (solid red lines) and unstable (dashed blue lines) steady-state solutions as a function of α/β_1 for a fixed $\tau_3/\tau_1=0.7$, corresponding to the line ACF in Fig. 4 (see inset). The input power is the critical power P_{crit} , so there is always a 100%-efficiency stable solution, but as α/β_1 increases new stable and unstable solutions appear at lower efficiencies.

to have a smaller and smaller basin of attraction as α/β_1 increases, making it harder to excite as described in the next section. The next two plots, in Fig. 7, both show the solutions with respect to changes in τ_3/τ_1 at two different values of α/β_1 . They demonstrate that at $\tau_1=\tau_3$, a Hopf bifurcation occurs where the 100%-efficiency solution becomes unstable for $\tau_3 \geq \tau_1$ and limit cycles appear, intuitively seeming to “bounce between” the two nearby unstable fixed points. (The actual phase space is higher dimensional, however, so the limit cycles are not constrained to lie strictly between the efficiencies of the two unstable solutions.) It is worth noting

that the remaining nonzero-efficiency stable solution (which appears at a nonzero τ_3/τ_1) becomes less efficient as τ_3/τ_1 increases.

The above analysis and results were for the steady-state solutions when operating at the critical input power to obtain a 100%-efficiency solution. However, one can, of course, operate with a different input power—although no other input power will yield a 100%-efficient steady-state solution, different input powers may still be useful because (as noted above and in the next section) the 100%-efficiency solution may be unstable or practically unattainable. Figure 8 (left) is the bifurcation diagram with respect to the input power $P_{\text{in}}/P_{\text{crit}}$ at fixed α/β_1 and fixed τ_3/τ_1 , corresponding to point C in Fig. 4. This power bifurcation diagram displays a number of interesting features, with the steady-state solutions transitioning several times from stable to unstable and vice versa. As we will see in the next section, the stability transitions in the uppermost branch are actually supercritical (reversible) Hopf bifurcations to/from limit cycles. Near the critical power, there is only a small region of stability of the near-100% efficiency solution, as shown in the inset of Fig. 8 (left). In contrast, the lower-efficiency stable solutions have much larger stable regions of the curve while still maintaining efficiencies greater than 70% at low powers comparable to $P_{\text{crit}} \sim V/Q^2$, which suggests that they may be attractive regimes for practical operation when α/β_1 is not small. This is further explored in the next section, and also by Fig. 8 (right) which shows the bifurcation diagram along the line ACF in Fig. 4 [similar to Fig. 6], but at 135% of the critical input power. For this higher power, the system becomes at most doubly stable as α/β_1 is increased, and the higher-efficiency stable solution becomes surprisingly close to 100% as $\alpha/\beta_1 \rightarrow 0$.

IV. EXCITING HIGH-EFFICIENCY SOLUTIONS

One remaining concern in any multistable system is how to excite the desired solution—depending on the initial con-

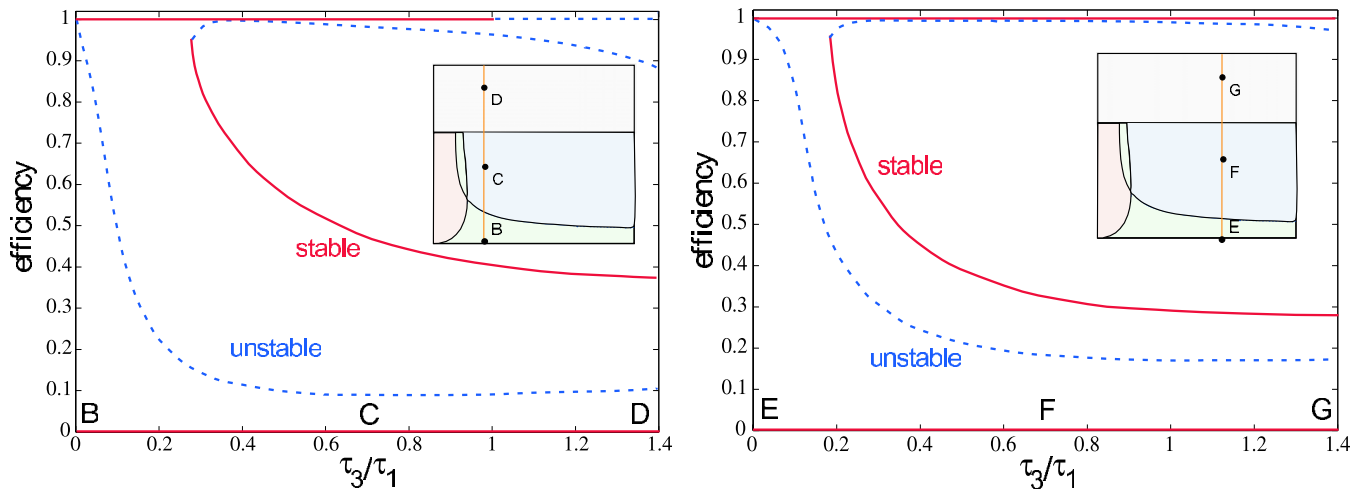


FIG. 7. (Color online) Bifurcation diagram showing the harmonic-generation efficiency of the stable (solid red lines) and unstable (dashed blue lines) steady-state solutions as a function of τ_3/τ_1 for a fixed $\alpha/\beta_1=3$ (left) or $=8$ (right), corresponding to the lines BCD or EFG, respectively, in Fig. 4 (see insets). The input power is the critical power $|s_{1\pm}|^2$, so there is always a 100%-efficiency steady-state solution, but it becomes unstable for $\tau_3 > \tau_1$ (a Hopf bifurcation leading to limit cycles as in Fig. 5).

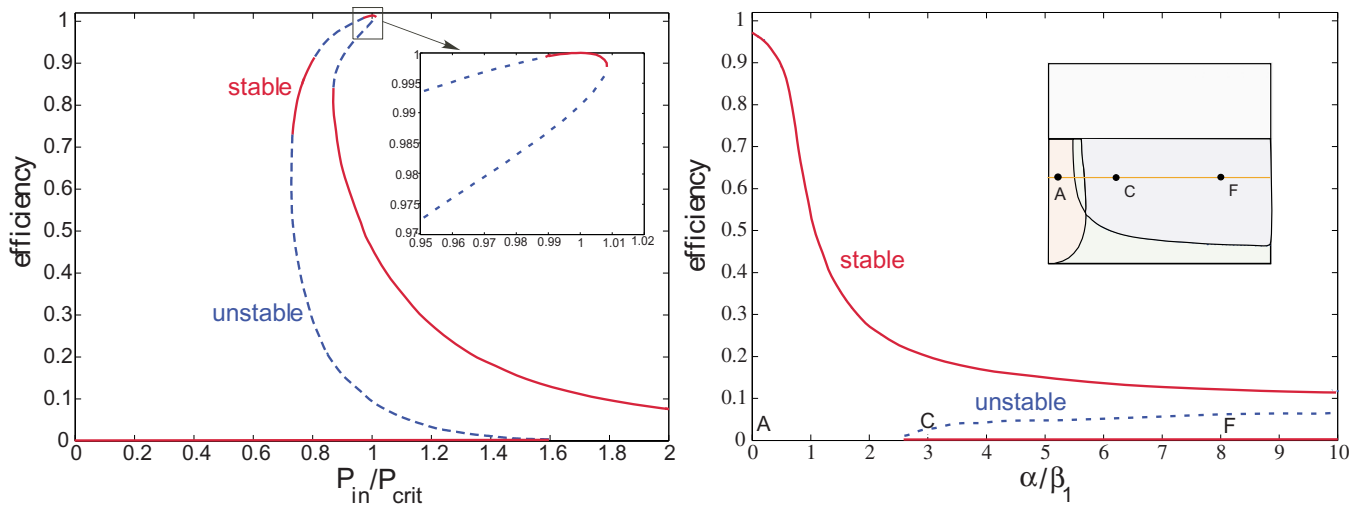


FIG. 8. (Color online) Left: Bifurcation diagram showing the harmonic-generation efficiency of the stable (solid red lines) and unstable (dashed blue lines) steady-state solutions as a function of P_{in}/P_{crit} at fixed $\alpha/\beta_1=3$ and $\tau_3/\tau_1=0.7$, corresponding to point C in Fig. 4; the inset shows an enlarged view of the high-efficiency solutions. Right: Bifurcation diagram as a function of α/β_1 for fixed $P_{in}/P_{crit}=1.35$ and fixed $\tau_3/\tau_1=0.7$; in this case, because it is not at the critical power, there are no 100%-efficiency solutions.

ditions, the system may fall into different stable solutions, and simply turning on the source at the critical input power may result in an undesired low-efficiency solution. If α/β_1 is small enough, of course, then from Fig. 4 the high-efficiency solution is the only stable solution and the system must inevitably end up in this state no matter how the critical power is turned on. Many interesting physical systems will correspond to larger values of α/β_1 , however [1], and in this case the excitation problem is complicated by the existence of other stable solutions. Moreover, the basins of attraction of each stable solution may be very complicated in the phase space, as illustrated by Fig. 9, where varying the initial cavity amplitudes $A_{1,3}$ from the 100%-efficiency solution causes the steady state to oscillate in a complicated way between the three stable solutions (at point C in Fig. 4). We have investigated several solutions to this excitation problem, and found an “adiabatic” excitation technique that reliably produces the high-efficiency solution without unreasonable sensitivity to the precise excitation conditions.

First, we considered a simple technique similar to the one described in Ref. [2] for exciting different solutions of a bistable filter: as shown in Fig. 10, we “turn on” the input power by superimposing a gradual exponential turn-on (asymptoting to $P_1=P_{crit}$) with a Gaussian pulse of amplitude P_0 and width δT . The function of the initial pulse is to “kick” the system into the desired stable solution. We computed the eventual steady-state efficiency (after all transient effects have disappeared) as a function of the pulse amplitude P_0 at point C in Fig. 4, where there are three stable solutions. The results are shown in Fig. 11 (left), and indeed we see that all three stable solutions from point C in Fig. 6: one at near-zero efficiency, one at around 47% efficiency, and one at 100% efficiency. Unfortunately, the 100% efficiency solution is obviously rather difficult to excite, since it occurs for only a very narrow range of P_0 values. One approach to dealing with this challenge is to relax the requirement of 100% efficiency (which will never be obtained in practice anyway due

to losses), and operate at a $P_1 < P_{crit}$. In particular, Fig. 8 (left) shows that there is a much larger stable region for $P_1 \approx 0.8P_{crit}$ with efficiency around 90%, leading one to suspect that this solution may be easier to excite than the 100%-efficiency solution at $P_1=P_{crit}$. This is indeed the case, as is shown in Fig. 11 (right), plotting efficiency vs P_0 at point C with $P_1 \approx 0.8P_{crit}$. In this case, there are only two stable solutions, consistent with Fig. 8 (left), and there are much wider ranges of P_0 that attain the high-efficiency ($\approx 90\%$) solution.

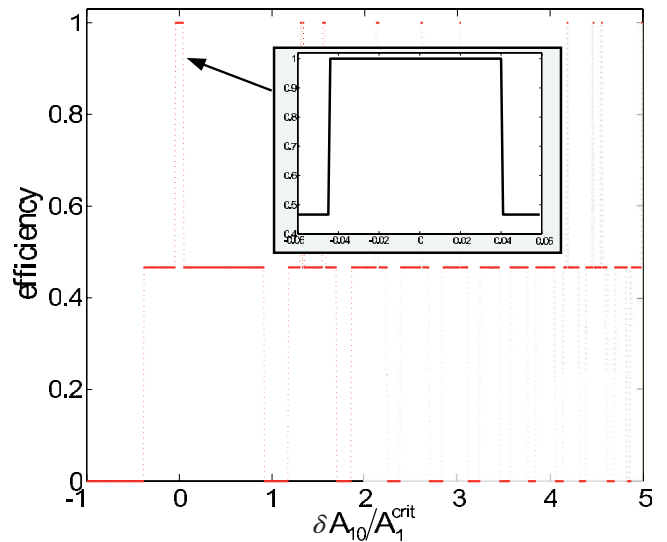


FIG. 9. (Color online) Asymptotic steady-state efficiency at point C (triple stable) in the phase diagram (Fig. 4), with the initial conditions perturbed from the 100%-efficiency stable solution. The initial amplitudes A_{10} and A_{30} are perturbed by δA_{10} and δA_{30} , respectively, with $\delta A_{10}/A_1^{crit} = \delta A_{30}/A_3^{crit}$. The oscillation of the steady-state efficiency with the perturbation strength is an indication of the complexity of the phase space and the shapes of the basins of attraction of each fixed point.

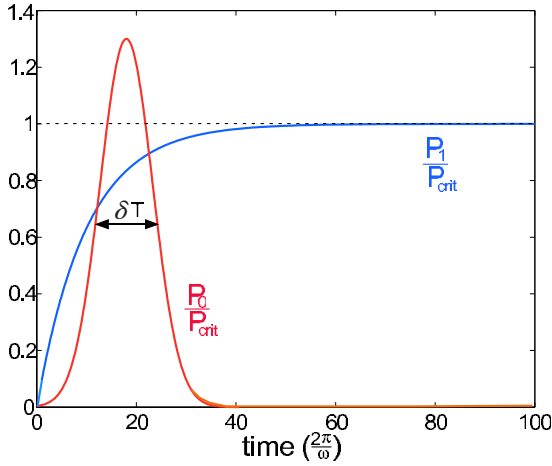


FIG. 10. (Color online) One way of exciting the system into a controlled stable solution: the input power is the sum of an exponential turn-on (the blue curve, P_1) and a Gaussian pulse with amplitude P_0 and width δT . The amplitude P_0 is altered to control which stable solution the system ends up in.

There are also many other ways to excite the high-efficiency solution (or whatever steady-state solution is desired). For example, because the cavity is initially detuned from the input frequency, as described in Sec. II, much of the initial pulse power is actually reflected during the transient period, and a more efficient solution would vary the pulse frequency in time to match the cavity frequency as it detunes. One can also, of course, vary the initial pulse width or shape, and by optimizing the pulse shape one may obtain a more robust solution.

In particular, one can devise a different (constant-frequency) input pulse shape that robustly excites the high-efficiency solution, insensitive to small changes in the initial conditions, by examining the power-bifurcation diagram in Fig. 8 (left) in more detail. First, we observe that for $P_{in} \gtrsim 1.45P_{crit}$ there is only one stable solution, meaning that this stable solution is excited regardless of the initial condi-

tions or the manner in which the input power is turned on. Then, if we slowly decrease the input power, the solution must “adiabatically” follow this stable solution in the bifurcation diagram until $P_{in} \approx 0.95P_{crit}$ is reached, at which point that stable solution disappears. In fact, by inspection of Fig. 8 (left), at that point there are *no* stable solutions, and solution jumps into a limit cycle. If the power is further decreased, a high-efficiency stable solution reappears and the system must drop into this steady state (being the only stable solution at that point). This process of gradually decreasing the power is depicted in Fig. 12 (left), where the instantaneous “efficiency” is plotted as a function of input power, as the input power is slowly decreased. (The efficiency can exceed unity, because we are plotting instantaneous output vs input power, and in the limit-cycle self-pulsing solution the output power is concentrated into pulses whose peak can naturally exceed the average input or output power.) Already, this is an attractive way to excite a high-efficiency ($>90\%$) solution, because it is insensitive to the precise manner in which we change the power as long as it is changed slowly enough—this rate is determined by the lifetime of the cavity, and since this lifetime is likely to be subnanosecond in practice, it is not difficult to change the power “slowly” on that timescale. However, we can do even better, once we attain this high-efficiency steady state, by then increasing the power adiabatically. As we increase the power, starting from the high-efficiency steady-state solution below the critical power, the system first enters limit-cycle solutions when the power becomes large enough that the stable solution disappears in Fig. 8 (right). As we increase the power further, however, we observe that these limit cycles always converge adiabatically into the 100%-efficiency solution when $P \rightarrow P_{crit}$. This process is shown in Fig. 12 (right). What is happening is actually a supercritical Hopf bifurcation at the two points where the upper branch changes between stable and unstable: this is a reversible transition between a stable solution and a limit cycle (initially small oscillations, growing larger and larger away from the transition). This is precisely what we observe in Fig. 12, in which the limit cycle

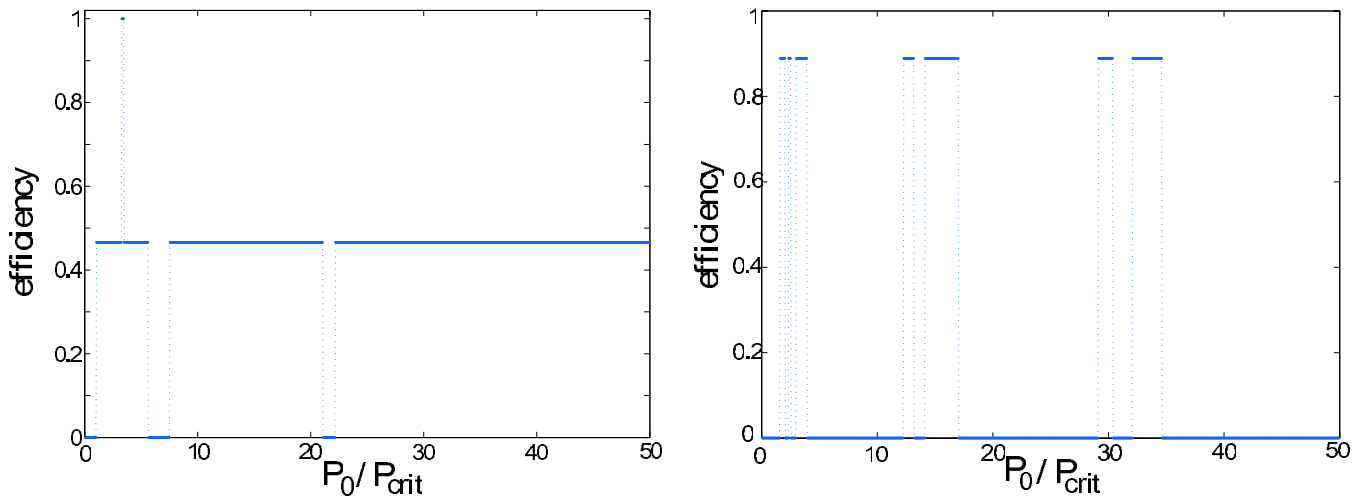


FIG. 11. (Color online) Left: Steady-state efficiency at point C in Fig. 4 as a function of the transient input-pulse amplitude P_0 from Fig. 10, showing how all three stable solutions can be excited by an appropriate input-pulse amplitude. Right: Same, but for an asymptotic input power $P_1 \approx 0.8P_{crit}$, for which the maximum efficiency is $\approx 90\%$ from Fig. 8 (right), but is easier to excite.

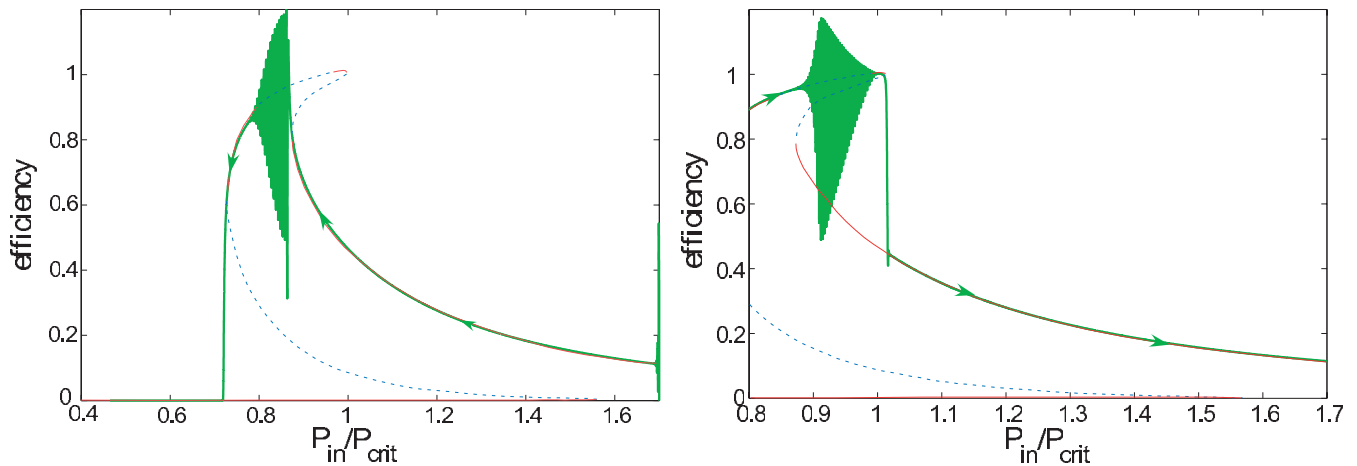


FIG. 12. (Color) Left: Green line with arrows indicates instantaneous “efficiency” (harmonic output power / input power) as the input power is slowly decreased, starting at $P_{\text{in}} \approx 1.7P_{\text{crit}}$. For comparison, Fig. 8 (left) is superimposed as solid-red and dashed-blue lines. The solution “adiabatically” follows a steady state until the steady state becomes unstable, at which point it enters limit cycles, and then returns to a high-efficiency steady state, and finally drops to a low-efficiency steady state if the power is further decreased. Right: Similar, but here the power is increased starting at the high-efficiency steady state for $P < P_{\text{crit}}$. In this case, it again enters limit cycles, but then it returns to a high-efficiency steady-state solution as the power is further increased, eventually reaching the 100%-efficiency stable solution. If the power is further increased, it drops discontinuously to the remaining lower-efficiency steady-state stable solution.

amplitudes become smaller and smaller as the stable solutions on either side of the upper branch are approached, leading to the observed reversible transitions between the two. The important fact is that, in this way, by first decreasing and then increasing P_{in} toward P_{crit} , one always obtains the 100%-efficiency solution regardless of the precise details of how the power is varied (as long as it is “slow” on the time scale of the cavity lifetime).

V. CONCLUDING REMARKS

We have shown that a doubly resonant cavity not only has high-efficiency harmonic conversion solutions for low input power, as in our previous work [1], but also exhibits a number of other interesting phenomena. We showed under what conditions the high-efficiency solution is stable, how to compensate for self-phase modulation, the existence of different regimes of multistable solutions and limit cycles controlled by the parameters of the system and by the input power, and how to excite the desired high-efficiency solution. Although we did not observe chaos, it seems possible that this may be obtained in future work for other parameter regimes, e.g., for pulsed input power as was observed in the $\chi^{(2)}$ case [4,5]. These dynamical phenomena depend only on certain dimensionless quantities α/β_1 , ω_3/ω_1 , τ_3/τ_1 , and $s_{1+}/s_{1+}^{\text{crit}}$, although the overall power and time scales depend upon the dimensional quantities $\tau_{1,3}$ and so on.

All of the calculations in this paper were for an idealized lossless system, as our main intention was to examine the fundamental dynamics of these systems rather than a specific experimental realization. However, we have performed preliminary calculations including both linear losses (such as radiation or material absorption) and nonlinear two-photon absorption, and we find that these losses do not qualitatively change the observed phenomena. One still obtains multista-

bility, limit cycles, bifurcations, and so on, merely at reduced peak efficiency depending on the strength of the losses. In a future manuscript, we plan to explore these effects in more detail in realistic material settings, and propose specific geometries to obtain the requisite doubly resonant cavities. In particular, to obtain widely spaced resonant modes ω and 3ω in a nanophotonic (wavelength-scale) context (as opposed to macroscopic Fabry-Perot cavities with mirrors), the most promising route seems to be a ring resonator of some sort [48], rather than a photonic crystal [30] (since photonic band gaps at widely separated frequencies are difficult to obtain in two or three dimensions). Although such a cavity will naturally support more than the two ω_1 and ω_3 modes, only two of the modes will be properly tuned to achieve the resonance condition for strong nonlinear coupling.

Finally, we should mention that similar phenomena should also arise in doubly and triply resonant cavities coupled nonlinearly by sum or difference frequency generation (for $\chi^{(2)}$) or four-wave mixing (for $\chi^{(3)}$). The advantage of this is that the coupled frequencies can lie closer together, imposing less stringent materials constraints and allowing the cavity to be confined by narrow-bandwidth mechanisms such as photonic band gaps [30], at the cost of a more complicated cavity design.

ACKNOWLEDGMENTS

This research was supported in part by the Army Research Office through the Institute for Soldier Nanotechnologies under Contract No. W911NF-07-D-0004. This work was also supported in part by a Department of Energy (DOE) Computational Science Fellowship under Grant No. DE-FG02-97ER25308 (AWR). We are also grateful to A. P. McCauley at MIT and S. Fan at Stanford for helpful discussions.

APPENDIX

As explained in the text, enforcing the steady state condition on Eqs. (1) and (2) yields a set of coupled polynomial equations, whose roots we compute using MATHEMATICA. However, some transformations were required in order to put the equations into a solvable form.

In particular, we eliminated the complex conjugations by writing $A_k = r_k e^{i\phi_k}$ and assuming (without loss of generality) that s_{1+} is real. Multiplying Eq. (1) by $e^{-i\phi_1}$ and Eq. (2) by $e^{-i3\phi_1}$ allows us to simply solve the system for $e^{-i\phi_1}$ and $e^{i(\phi_3-3\phi_1)}$:

$$e^{i\phi_3} = \frac{i\omega_3\beta_3r_1^3}{r_3\left(i\{\omega_3^{\text{cav}}[1-\alpha(r_1^2+r_3^2)]-\omega_3\}-\frac{1}{\tau_3}\right)}$$

$$e^{i(\phi_3-3\phi_1)} = \frac{r_1}{s_{1+}} \left[\frac{-\omega_1\omega_3\beta_1\beta_3r_1^4}{i[\omega_3^{\text{cav}}-\omega_3-\omega_3^{\text{cav}}\alpha(r_1^2+r_3^2)]-1/\tau_3} + i[\omega_1^{\text{cav}}-\omega_1+\omega_1^{\text{cav}}\alpha(r_1^2+r_3^2)]+1/\tau_1 \right]. \quad (\text{A1})$$

Requiring the magnitude of these two quantities to be

unity yields two polynomials in $x=r_1^2$ and $y=r_3^2$, which MATHEMATICA can handle:

$$0 = \omega_3^2\beta_3^2x^3 - (1/\tau_3^2 + \{\omega_3^{\text{cav}}[1-\alpha(x+y)]-\omega_3\}^2)y$$

$$0 = 1/\tau_3^2 + \{\omega_3^{\text{cav}}[1-\alpha(x+y)]-\omega_3\}^2 - \frac{x}{s_{1+}^2} \left[\left(-\omega_1\omega_3\beta_1\beta_3x^2 - \frac{1}{\tau_1\tau_3} + \{\omega_3^{\text{cav}}[1-\alpha(x+y)]-\omega_3\}\{\omega_1^{\text{cav}}[1-\alpha(x+y)] - \omega_1\}^2 + \left(\frac{\omega_3^{\text{cav}}[1-\alpha(x+y)]-\omega_3}{\tau_1} + \frac{\omega_1^{\text{cav}}[1-\alpha(x+y)]-\omega_1}{\tau_3} \right)^2 \right] \right]. \quad (\text{A2})$$

The resulting polynomial is of an artificially high degree, resulting in spurious roots, but the physical solutions are easily identified by the fact that x and y must be real and non-negative. (We should also note that this root-finding process is highly sensitive to roundoff error [49], independent of the physical stability of the solutions, but we dealt with that problem by employing 50 decimal places of precision.)

-
- [1] A. Rodriguez, M. Soljačić, J. D. Joannopoulos, and S. G. Johnson, *Opt. Express* **15**, 7303 (2007).
- [2] M. Soljačić, M. Ibanescu, S. G. Johnson, Y. Fink, and J. D. Joannopoulos, *Phys. Rev. E* **66**, 055601(R) (2002).
- [3] R. S. Tasgal Y. B. Band, and B. A. Malomed, *Phys. Rev. E* **72**, 016624 (2005).
- [4] P. D. Drummond, K. J. McNeil, and D. F. Walls, *Opt. Acta* **27**, 321 (1980).
- [5] K. Grygiel and P. Szałcietka, *Opt. Commun.* **91**, 241 (1992).
- [6] J. A. Armstrong, N. Loembergen, J. Ducuing, and P. S. Pershan, *Phys. Rev.* **127**, 1918 (1962).
- [7] A. Ashkin, G. D. Boyd, and J. M. Dziedzic, *IEEE J. Quantum Electron.* **2**, 109 (1966).
- [8] R. G. Smith, *IEEE J. Quantum Electron.* **6**, 215 (1970).
- [9] A. Ferguson and M. H. Dunn, *IEEE J. Quantum Electron.* **13**, 751 (1977).
- [10] M. Brieger, H. Busener, A. Hese, F. V. Moers, and A. Renn, *Opt. Commun.* **38**, 423 (1981).
- [11] J. C. Bergquist, H. Hemmati, and W. M. Itano, *Opt. Commun.* **43**, 437 (1982).
- [12] W. J. Kozlovsky, W. P. Risk, W. Lenth, B. G. Kim, G. L. Bona, H. Jaekel, and D. J. Webb, *Appl. Phys. Lett.* **65**, 525 (1994).
- [13] G. J. Dixon, C. E. Tanner, and C. E. Wieman, *Opt. Lett.* **14**, 731 (1989).
- [14] M. J. Collet and R. B. Levien, *Phys. Rev. A* **43**, 5068 (1991).
- [15] M. A. Persaud, J. M. Tolchard, and A. I. Ferguson, *IEEE J. Quantum Electron.* **26**, 1253 (1990).
- [16] G. T. Moore, K. Koch, and E. C. Cheung, *Opt. Commun.* **113**, 463 (1995).
- [17] K. Schneider, S. Schiller, and J. Mlynek, *Opt. Lett.* **21**, 1999 (1996).
- [18] X. Mu, Y. J. Ding, H. Yang, and G. J. Salamo, *Appl. Phys. Lett.* **79**, 569 (2001).
- [19] J. Hald, *Opt. Commun.* **197**, 169 (2001).
- [20] G. McConnell, A. I. Ferguson, and N. Langford, *J. Phys. D* **34**, 2408 (2001).
- [21] T. V. Dolgova, A. I. Maidikovski, M. G. Martemyanov, A. A. Fedyanin, O. A. Aktsipetrov, G. Marowsky, V. A. Yakovlev, G. Mattei, N. Ohta, and S. Nakabayashi, *J. Opt. Soc. Am. B* **19**, 2129 (2002).
- [22] T.-M. Liu, C.-T. Yu, and C.-K. Sun, *Appl. Phys. Lett.* **86**, 061112 (2005).
- [23] L. Scaccabarozzi, M. M. Fejer, Y. Huo, S. Fan, X. Yu, and J. S. Harris, *Opt. Lett.* **31**, 3626 (2006).
- [24] C. C. Gerry, *Phys. Rev. A* **59**, 4095 (1999).
- [25] M. A. Nielsen and I. L. Chuang, *Quantum Computation and Quantum Information* (Cambridge University Press, Cambridge, 2000).
- [26] T. J. Kippenberg, S. M. Spillane, and K. J. Vahala, *Phys. Rev. Lett.* **93**, 083904 (2004).
- [27] K. Nemoto and W. J. Munro, *Phys. Rev. Lett.* **93**, 250502 (2004).
- [28] P. Bermel, A. Rodriguez, S. G. Johnson, J. D. Joannopoulos, and M. Soljačić, *Phys. Rev. A* **74**, 043818 (2006).
- [29] R. W. Boyd, *Nonlinear Optics* (Academic Press, California, 1992).
- [30] J. D. Joannopoulos, S. G. Johnson, J. N. Winn, and R. D. Meade, *Photonic Crystals: Molding the Flow of Light*, 2nd ed. (Princeton University Press, Princeton, 2008).
- [31] R. Paschotta, K. Fiedler, P. Kurz, and J. Mlynek, *Appl. Phys. B* **58**, 117 (1994).
- [32] V. Berger, *J. Opt. Soc. Am. B* **14**, 1351 (1997).

- [33] I. Zolotoverkh, N. V. Kravtsov, and E. G. Lariontsev, *Quantum Electron.* **30**, 565 (2000).
- [34] B. Maes, P. Bienstman, and R. Baets, *J. Opt. Soc. Am. B* **22**, 1378 (2005).
- [35] M. Liscidini and L. C. Andreani, *Phys. Rev. E* **73**, 016613 (2006).
- [36] Y. Dumeige and P. Feron, *Phys. Rev. A* **74**, 063804 (2006).
- [37] L.-A. Wu, M. Xiao, and H. J. Kimble, *J. Opt. Soc. Am. B* **4**, 1465 (1987).
- [38] Z. Y. Ou and H. J. Kimble, *Opt. Lett.* **18**, 1053 (1993).
- [39] S. Schiller, Ph.D. thesis, Stanford University, Stanford, CA, 1993.
- [40] E. Abraham, W. J. Firth, and J. Carr, *Phys. Lett. A* **91**, 47 (1982).
- [41] A. Parini, G. Bellanca, S. Trillo, M. Conforti, A. Locatelli, and C. De Angelis, *J. Opt. Soc. Am. B* **24**, 2229 (2007).
- [42] A. Siegman, *Lasers* (University Science Books, Mill Valley, CA, 1986).
- [43] M. Notomi, A. Shinya, S. Mitsugi, G. Kira, E. Kuramochi, and T. Tanabe, *Opt. Express* **13**, 2678 (2005).
- [44] F. S. Felber and J. H. Marburger, *Appl. Phys. Lett.* **28**, 731 (1976).
- [45] W. Suh, Z. Wang, and S. Fan, *IEEE J. Quantum Electron.* **40**, 1511 (2004).
- [46] M. Tabor, *Chaos and Integrability in Nonlinear Dynamics: An Introduction* (Wiley, New York, 1989).
- [47] S. H. Strogatz, *Nonlinear Dynamics and Chaos* (Westview Press, Boulder, CO, 1994).
- [48] B. E. A. Saleh and M. C. Teich, *Fundamentals of Photonics* (Wiley, New York 1991).
- [49] W. H. Press, S. A. Teukolsky, W. T. Vetterling, and B. P. Flannery, *Numerical Recipes in C: The Art of Scientific Computing*, 2nd ed. (Cambridge University Press, Cambridge, 1992).